Evolution of the Rembrandt Impact Basin on Mercury

Thomas R. Watters, *et al.*

Science **324**, 618 (2009);
DOI: 10.1126/science.1172109

Science (print ISSN 0036-8075; online ISSN 1095-9203) is published weekly, except the last week in December, by the American Association for the Advancement of Science, 1200 New York Avenue NW, Washington, DC 20005.

27. W. E. McClintock *et al.*, *Science* **324**, 610 (2009).
28. B. Rava, B. Hapke, *Icarus* **71**, 397 (1987).
29. D. T. Blewett *et al.*, *Earth Planet. Sci. Lett.*, 10.1016/j.epsl.2009.02.021 (2009).
30. V. J. Hillgren, C. K. Gessman, J. Li, in *Origin of the Earth and Moon*, R. M. Canup, K. Righter, Eds. (Univ. Arizona Press, Tucson, 2000), pp. 245–263.
31. M. A. Riner, P. G. Lucey, S. J. Desch, F. M. McCubbin, *Geophys. Res. Lett.* **36**, L02201 (2009).
32. B. Hapke, *Theory of Reflectance and Emittance Spectroscopy: Topics in Remote Sensing 3* (Cambridge Univ. Press, New York, 1993).
33. D. J. Lawrence, W. C. Feldman, J. O. Goldsten, *Lunar Planet. Sci.* **40**, abstr. 1761 (2009).
34. T. M. Usselman, G. E. Lofgren, C. H. Donaldson, R. J. Williams, *Proc. Lunar Sci. Conf.* **6**, 997 (1975).
35. A. G. W. Cameron, *Icarus* **64**, 285 (1985).
36. W. Benz, W. L. Slattery, A. G. W. Cameron, *Icarus* **74**, 516 (1988).
37. S. E. Hawkins III *et al.*, *Space Sci. Rev.* **131**, 247 (2007).
38. M. J. Cintala, R. A. F. Grieve, *Meteorit. Planet. Sci.* **33**, 889 (1998).
39. We gratefully acknowledge the MESSENGER engineers and technical support team. N. Laslo, H. Kang, R. Vaughan, A. Harch, R. Shelton, and A. Berman designed the imaging sequences used here. S. Turner, K. Becker, and C. Hash contributed to data calibration and processing. The MESSENGER project is supported by the NASA Discovery Program under contracts NAS5-97271 to the Johns Hopkins University Applied Physics Laboratory and NASW-00002 to the Carnegie Institution of Washington.

12 February 2009; accepted 8 April 2009
10.1126/science.1172226

Evolution of the Rembrandt Impact Basin on Mercury

Thomas R. Watters,[1]* James W. Head,[2] Sean C. Solomon,[3] Mark S. Robinson,[4] Clark R. Chapman,[5] Brett W. Denevi,[4] Caleb I. Fassett,[2] Scott L. Murchie,[6] Robert G. Strom[7]

MESSENGER's second Mercury flyby revealed a ~715-kilometer-diameter impact basin, the second-largest well-preserved basin-scale impact structure known on the planet. The Rembrandt basin is comparable in age to the Caloris basin, is partially flooded by volcanic plains, and displays a unique wheel-and-spoke–like pattern of basin-radial and basin-concentric wrinkle ridges and graben. Stratigraphic relations indicate a multistaged infilling and deformational history involving successive or overlapping phases of contractional and extensional deformation. The youngest deformation of the basin involved the formation of a ~1000-kilometer-long lobate scarp, a product of the global cooling and contraction of Mercury.

Impact basins, generally in excess of several hundred kilometers in diameter, are among the most important landforms created early in planetary history (*1*). Because of their typically ancient ages, most basins have been modified and filled with volcanic plains, which obscure their initial state and early evolution. A few basins, such as Orientale on the Moon, remain largely unfilled and provide substantial insight into basin formation and early modification (*2*, *3*). During its second flyby of Mercury in October 2008, the MESSENGER spacecraft imaged ~30% of the planet not previously seen by spacecraft. These images revealed a relatively unmodified basin centered near 33°S, 88°E (Fig. 1A). The interior of the basin, recently named Rembrandt, differs considerably from that of the well-preserved and larger Caloris basin, imaged by Mariner 10 (*4*, *5*) and during MESSENGER's first Mercury encounter (*6*–*11*). The Caloris basin contains substantial infill by plains of volcanic origin that cover its entire floor. On the basis of MESSENGER observations, we here assess the characteristics of the Rembrandt basin and their geological implications.

The Rembrandt basin (Fig. 1A) has a topographically distinct main rim crest made up of rugged, high-relief, inward-facing scarps and massifs. At ~715 km, its mean rim crest diameter is larger than the intermediate-scale, partly filled impact basins Beethoven (~625 km) and Tolstoj (~510 km) (*5*) and about half the size of the largest known basin, Caloris (>1500 km) (*7*, *8*). Numerous large impact craters are superposed on the rim of the basin (Fig. 1A). The number of craters ≥20 km in diameter per million square kilometers is not distinguishable from that for the rim of the Caloris basin [see supporting online material (SOM), figs. S1 to S3]. The crater size-frequency distribution (SFD) for the Rembrandt basin rim (Fig. 1B) is also similar to that for the Caloris basin rim (*11*). These results suggest that Rembrandt, like Caloris, is one of the youngest basins on Mercury, younger than Tolstoj and Beethoven, yet sufficiently old to show the pattern of fewer small-diameter craters relative to large-diameter craters that is characteristic of terrains formed before the end of the late heavy bombardment of the inner solar system (~3.9 billion years ago) (*12*).

Exterior to the basin rim crest are blocky and radially lineated ejecta deposits, well preserved to the north and northeast of the basin rim, respectively (Fig. 1, A and C). These deposits are comparable to the annuli of radially textured ejecta outside the rims of the Caloris basin (*5*, *11*) and the lunar Orientale basin (*2*, *3*). Basin interior units include a hummocky unit and a smooth plains unit. The hummocky unit extends inward from the basin rim by up to ~130 km (Fig. 1D) and is distinguished by knobs that rise up to hundreds of meters (from shadow measurements) above patches of rolling hills near the basin margin (Fig. 1C). This unit forms a discontinuous ring in the basin interior, confined to the northern margin. Two large, angular blocks or massifs on the southern edge of the hummocky unit have a maximum relief of >1.5 km (Fig. 1D). The inner edge of the hummocky unit and the massifs may mark the remnants of a ringlike structure with a diameter of ~450 km (Figs. 1 and 2). The hummocky and domical morphology of the unit and its position just inside the basin rim are similar to those of the Montes Rook Formation in Orientale, interpreted to have been formed by collapse and inward translation of the transient cavity rim and modification of radially textured rim deposits into domical blocks (*2*, *3*). This interpretation is supported by remnant radial crater-chain–like structures (Fig. 1D), similar to occurrences in Orientale, and suggests that the inner edge and massifs of this unit delineate the remnant of the transient cavity rim (*2*).

Smooth plains constitute the most areally extensive unit in the Rembrandt basin; occupy much of the basin interior; and extend to the southern, eastern, and parts of the western rim (Fig. 2A). In the lunar Orientale basin, non-mare smooth and rough plains inside the transient cavity are interpreted to be impact melt (*1*–*3*). On the basis of laboratory experiments and theoretical scaling arguments, the volume of impact melt formed in basins is predicted to increase with basin size and perhaps even to fill entirely the basin interior at the largest diameters (*13*). If the regional plains are impact melt, they would have been emplaced in the immediate aftermath of basin formation and collapse, before formation of any subsequent major impact craters, as has been documented for the lunar Orientale basin (*14*). Furthermore, they should have spectral characteristics appropriate for a physical mixture of the target materials.

Broadly distributed spectral units on Mercury identified from global principal component analysis and spectral ratios of MESSENGER's 11-color wide-angle camera (WAC) images include low-reflectance material (LRM), spectrally intermediate terrain, and three types of smooth plains: (i) high-reflectance red plains (HRP), (ii) intermediate plains, and (iii) low-reflectance blue plains (LBP) (*10*, *15*). Comparison of color data between the Rembrandt basin and other regions of the planet is complicated by the area's near-

[1]Center for Earth and Planetary Studies, National Air and Space Museum, Smithsonian Institution, Washington, DC 20560, USA. [2]Department of Geological Sciences, Brown University, Providence, RI 02912, USA. [3]Department of Terrestrial Magnetism, Carnegie Institution of Washington, Washington, DC 20015, USA. [4]School of Earth and Space Exploration, Arizona State University, Tempe, AZ 85251, USA. [5]Southwest Research Institute, 1050 Walnut Street, Boulder, CO 80302, USA. [6]Johns Hopkins University Applied Physics Laboratory, Laurel, MD 20723, USA. [7]Lunar and Planetary Laboratory, University of Arizona, Tucson, AZ 85721, USA.

*To whom correspondence should be addressed. E-mail: watterst@si.edu

terminator lighting and oblique viewing geometry during the flyby. Relative color and reflectance differences across the basin region show that ejecta and interior hummocky units of Rembrandt are lower in reflectance than the interior smooth plains (Fig. 3) and broadly similar spectrally to LRM and LBP. The high relative reflectance of the interior plains is analogous to that of HRP, interpreted to be of volcanic origin (*10*, *15*). Moreover, the exterior ejecta of several major craters in the interior smooth plains have been embayed by plains units (Fig. 2B), and there is evidence of breached rims and interior crater infilling by smooth plains (Fig. 2A), suggesting a prolonged period of plains formation. The distinct spectral

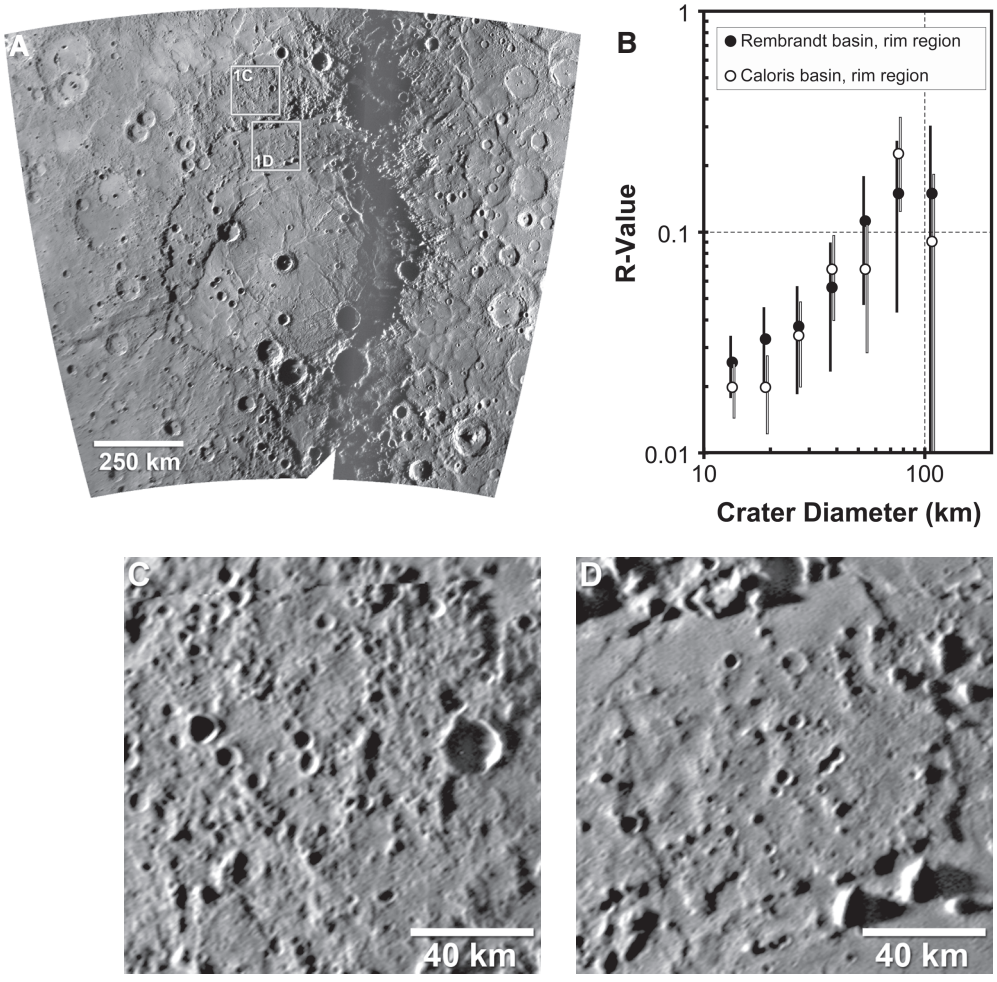

Fig. 1. The Rembrandt basin. (**A**) NAC mosaic (*24*) combining images obtained during MESSENGER's first and second flybys, including frames EN0108828198M, EN0108828203M, EN0108828250M, EN0108828255M, EN0108828302M, EN0108828307M, EN0131766380M, EN0131766396M, EN0131766401M, EN0131766417M, and EN0131766422M. White boxes outline areas shown in (C) and (D). (**B**) Impact crater SFD for the Rembrandt basin rim compared with that for the Caloris rim. This plot is an R plot (see SOM), a version of the differential crater SFD (*12*). Errors shown are inversely proportional to the square root of the number of craters in each crater-diameter interval. (**C**) Blocky terrain on the basin rim interpreted to be ejecta deposits. Image taken from NAC frame EN0131766417M. (**D**) Hummocky terrain in the basin interior made up of isolated knobs, interpreted to be ejecta deposits modified by basin collapse. Image taken from NAC frame EN0131766417M.

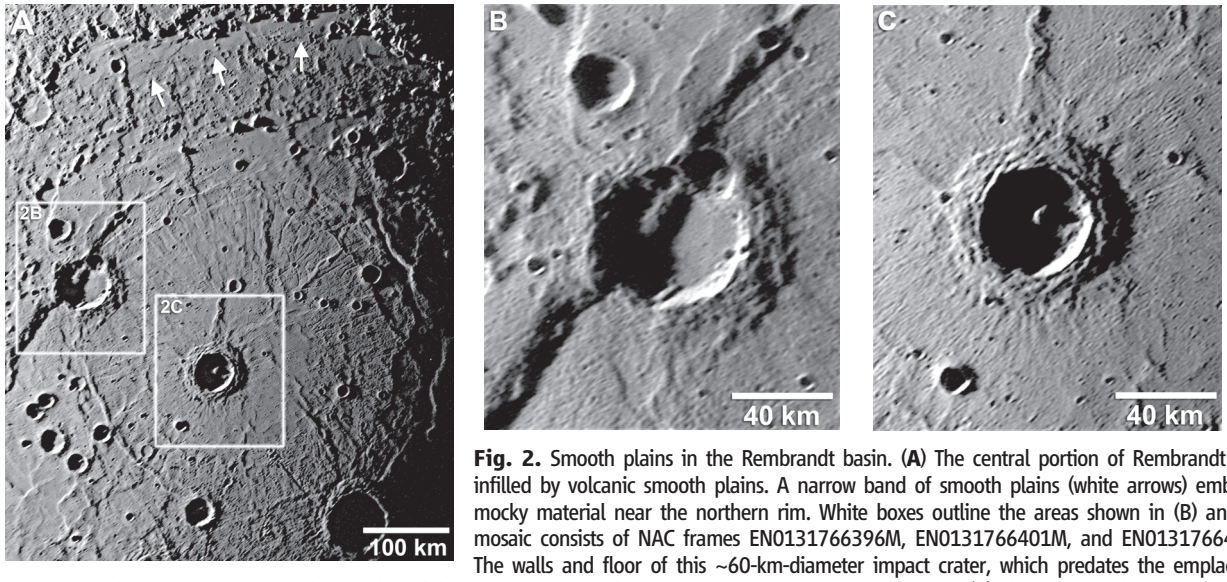

Fig. 2. Smooth plains in the Rembrandt basin. (**A**) The central portion of Rembrandt has been infilled by volcanic smooth plains. A narrow band of smooth plains (white arrows) embays hummocky material near the northern rim. White boxes outline the areas shown in (B) and (C). The mosaic consists of NAC frames EN0131766396M, EN0131766401M, and EN0131766417M. (**B**) The walls and floor of this ~60-km-diameter impact crater, which predates the emplacement of some of the volcanic plains, are cross-cut and offset by a lobate scarp. Image taken from NAC frame EN0131766396M. (**C**) This ~44-km-diameter impact crater postdates the emplacement of the smooth plains. Image taken from NAC frame EN0131766401M.

characteristics of the interior plains, the embayment relations between interior plains material and the interior hummocky deposits, and the embayed and partially flooded impact craters, all similar to relations seen in the Caloris basin interior (*7*–*9*), support a volcanic origin for the smooth plains material in the Rembrandt basin.

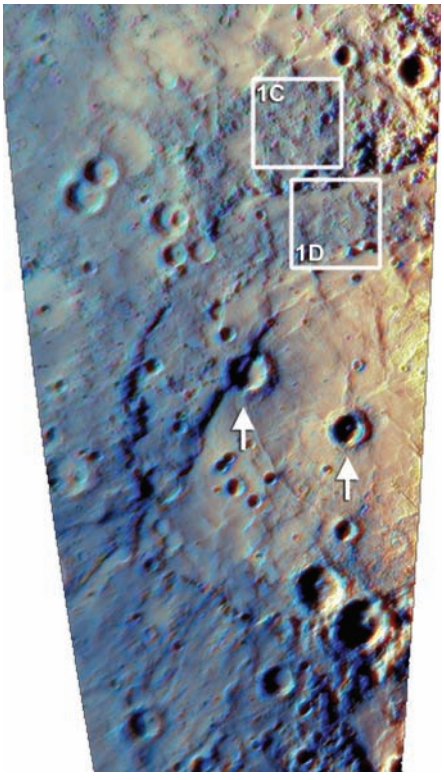

Fig. 3. Color composite of the spectral parameters used to separate units on the basis of principal component analysis of WAC 11-color images (*10*, *15*). The first principal component (PC1) emphasizes variations in reflectance, and the second principal component (PC2) emphasizes spectral variations related to the physical state or chemistry of the material. The dominant variation represented by PC2 is the slope of the spectral continuum. A color composite in which PC2, PC1, and the 430-nm/1000-nm reflectance ratio are shown in the red, green, and blue image planes, respectively, is overlaid on the NAC mosaic. White boxes show the locations of exterior ejecta (Fig. 1C, upper box) and interior ejecta and collapse deposits (Fig. 1D, lower box). White arrows indicate the locations of impact craters shown in Fig. 2B (left arrow) and Fig. 2C (right arrow). The spectral character of the interior plains (relatively high reflectance) differs from that of the ejecta and hummocky deposits (relatively low reflectance). The extreme incidence (>78°) and phase (>130°) angles for WAC images of the Rembrandt area (where the incidence angle is the angle between the direction to the Sun and the surface normal, and the phase angle is the angle between the solar incidence direction and the camera boresight direction at the planet's surface) complicate comparisons with color units elsewhere on the planet. Image taken from MDIS WAC approach color sequence (EW0131764500C to EW0131764550A).

The thickness of volcanic fill in the Rembrandt basin varies greatly. Along the northern interior, the hummocky deposit is embayed but not completely buried (Fig. 1C), suggesting a relatively thin sequence of volcanic plains in this area. Near the basin center, a ~44-km-diameter crater superposed on the smooth plains (Fig. 2, A and C, and Fig. 3) exhibits predominantly plains-like spectral material in its rim and ejecta, indicating that the underlying crust and basin material were not excavated and exposed (Figs. 2C and 3). Given a depth of excavation for complex craters of ~5% of the crater diameter, a lower bound on the thickness of the volcanic plains is ~2 km near the center of the basin, a thickness similar to that interpreted in the center of Caloris (*8*) and some lunar basins (*16*). The Rembrandt basin thus represents a stage of filling by presumably volcanic plains that is intermediate between those of the largely unfilled lunar Orientale basin, where mare basalts are patchy and considerably less than 1 km thick (*2*), and the Caloris and lunar Imbrium basins, where basin-interior ring structures and impact melt deposits are almost completely buried by volcanic infill (*1*, *3*, *7*–*10*).

The tectonic features in the Rembrandt basin show evidence for both basin-localized and global-scale deformation. Extensional troughs and wrinkle ridges are confined to the spectrally distinct, volcanic plains. Wrinkle ridges with orientations that are both basin-radial and basin-concentric are common (Figs. 2A and 4A) and are interpreted to be contractional features resulting from a combination of folding and thrust faulting (*17*–*19*). Basin-concentric wrinkle ridges form an almost complete ~375-km-diameter ring in the interior. This second ringlike structure is ~50 to 60 km inside the hummocky unit and massifs (Fig. 2A). Basin-radial wrinkle ridges occur both interior and exterior to this ring, although most of them are inside (Fig. 4, B and C). Their widths vary greatly (<1 to 10 km), and the longest ridges (one over 180 km) (Fig. 4C) form the interior ring. Basin-concentric and basin-radial wrinkle ridges are also found in Caloris (*7*, *8*) and in lunar maria (e.g., Imbrium, Serenitatis, Crisium) (*16*–*18*). In lunar maria, however, basin-concentric wrinkle ridges generally occur in the basin interior and basin-radial wrinkle ridges near the margins (*16*, *20*). In contrast, in the Rembrandt basin, many basin-radial wrinkle ridges occur interior to the concentric wrinkle ridges. The distinctive ring of ridges in the basin may reflect deformation localized by a buried interior basin ring, as is interpreted to be the case on the Moon (*17*).

The interior plains are cut by a series of linear and curvilinear troughs that also form a basin-radial and basin-concentric pattern (Figs. 2A and 4A). Of these, the basin-radial troughs are the most abundant and are located largely interior to the ring of wrinkle ridges (Fig. 2A and Fig. 4, B and C). Some of the radial troughs are adjacent and parallel to basin-radial ridges (Fig. 4, B and C). Unlike the radial troughs of Pantheon Fossae in Caloris that extend outward from a zone near the center of the basin (*7*, *8*), the radial graben of the Rembrandt basin are confined to a zone that extends inward less than ~100 km from the interior ridge ring. Some radial and concentric troughs in the basin form a polygonal pattern near the outer margin of the interior ridge ring (Fig. 4B), similar to the polygonal pattern formed by troughs near the margin of the Caloris basin (*7*, *8*). From the similarity of individual landforms as well as this similarity in distribution, we interpret the troughs in the Rembrandt basin to be graben, extensional features consisting of opposite-facing normal faults. Trough widths vary (<1 to ~3 km) but by a smaller range than in Caloris. The spatial distribution of these graben differs substantially from that in lunar basins, where graben tend to occur near the outer margins of the mare deposits or in adjacent highlands (*3*, *16*, *20*). The basin-radial graben and wrinkle ridges form a unique wheel-spoke pattern of tectonic landforms.

Episodes of contractional and extensional deformation in the basin are suggested by cross-cutting relations among the tectonic features. Radial and concentric graben cross-cut both basin-concentric and basin-radial wrinkle ridges (Fig. 4, B to D), indicating that much of the contractional deformation of the smooth plains preceded extensional deformation. This sequence of tectonic events is similar to that observed in Caloris (*7*, *8*). However, evidence that some concentric and radial wrinkle ridges cross-cut graben and older ridges indicates that the contraction and extension were not separated temporally into distinct deformational episodes (Fig. 4, B and D). Later contraction, for instance, may have been in response to a later stage of infilling by volcanic material in the center of the basin, as suggested by embayment relations between the more heavily deformed smooth plains inward of the ring of wrinkle ridges and the less deformed smooth plains (those lacking radial graben) near the basin center (Fig. 4B).

In parallel with scenarios invoked for the Caloris basin (*6*–*10*), effusive volcanism at some time after basin formation is inferred to have resulted in a thick sequence of volcanic material in the basin center. Loading by volcanic infill induced subsidence and near-surface compressional stresses that formed wrinkle ridges radial and concentric to the basin center in the interior smooth plains. Models of stresses in lunar mascon basins, however, predict a basin-radial pattern of wrinkle ridges far from the basin center (*21*). The formation of radial and concentric graben in the interior of the Rembrandt basin points to uplift of the basin floor and extension that postdated or perhaps overlapped interior loading. After uplift and extension of the basin floor, a later episode of volcanic infilling suggested by embayment relations in the basin center (Fig. 4B) could have resulted in renewed subsidence and contraction of the interior plains. One possible mechanism for basin floor uplift is inward flow of the lower crust driven by hori-

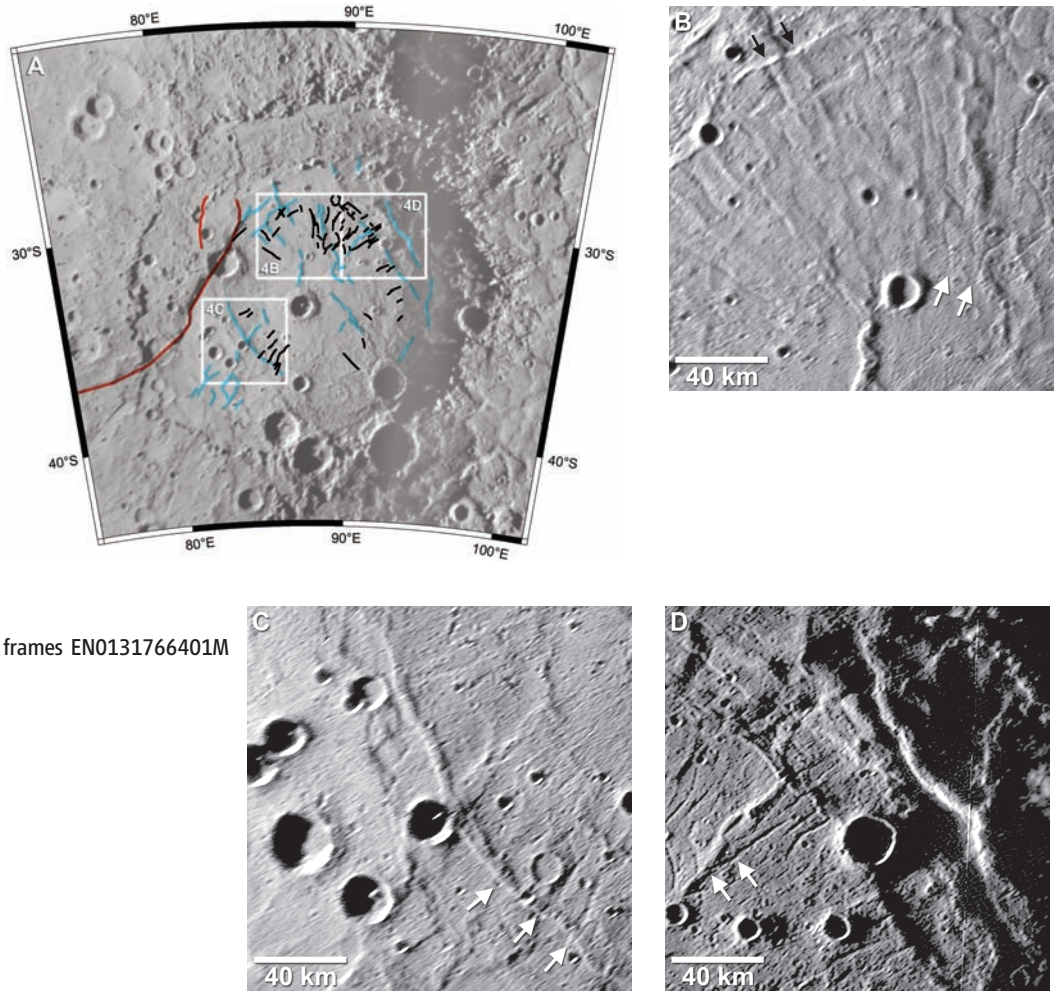

Fig. 4. (**A**) Map of tectonic features in the basin, including wrinkle ridges (blue), troughs or graben (black), and lobate scarps (red) digitized from and overlaid on a NAC mosaic. (**B**) In this complex pattern of wrinkle ridges and extensional troughs, some concentric wrinkle ridges are superposed on radial wrinkle ridges and graben (black arrows). Smooth plains material near the basin center appears to embay and partially bury plains cut by graben (white arrows). NAC mosaic includes frames EN0131766396M and EN0131766401M. (**C**) A basin-concentric wrinkle ridge, part of the interior ring of ridges, appears to be cross-cut by basin-radial graben (white arrows). NAC mosaic includes frames EN0131766401M and EN0131766417M. (**D**) A basin-radial wrinkle ridge appears to cross-cut a basin-radial graben (white arrows). NAC mosaic includes frames EN0131766401M and EN0108828250M.

zontal pressure gradients induced by differences in elevation and crustal thickness (*20*). Alternatively, loading by volcanic plains emplaced exterior to the basin could have led to flexural uplift of the basin interior (*22*, *23*).

Global tectonic evolution also influenced the region. The most recent event in the deformation of the basin appears to have been the formation of a cross-cutting lobate scarp, the longest yet documented on Mercury (Figs. 1A, 2B, and 4A). This lobate scarp, representative of a common tectonic landform interpreted as the surface expression of a major thrust fault (*4*), cuts the rim of the basin and extends nearly 400 km across the basin floor, offsetting the smooth plains material and the rims and floors of two ~60-km-diameter impact craters. The orientation of this northeast-southwest segment of the lobate scarp is approximately tangential to the interior ring of wrinkle ridges, suggesting that the buried interior ring surmised to underlie the ridge ring may also have influenced the thrust fault. The scarp extends for almost 600 km beyond the rim of the basin, cutting intercrater plains and transecting two other large impact craters. A second, shorter lobate scarp lies west of the northernmost segment of the large scarp and deforms interior smooth plains and hummocky material (Fig. 4A). Stresses produced by the global contraction that accompanied cooling of the planetary interior led to the formation of the lobate scarps that cut the rim and interior units of the basin and contributed to a stress regime less favorable to extrusive volcanism (*6*).

References and Notes

1. P. D. Spudis, *The Geology of Multi-Ring Impact Basins: The Moon and Other Planets* (Cambridge Univ. Press, New York, 1993).
2. J. W. Head, *Moon* **11**, 327 (1974).
3. D. E. Wilhelms, *U.S. Geol. Surv. Prof. Pap.* **1348**, 302 (1987).
4. R. G. Strom, N. J. Trask, J. E. Guest, *J. Geophys. Res.* **80**, 2478 (1975).
5. P. D. Spudis, J. E. Guest, in *Mercury*, F. Vilas, C. R. Chapman, M. S. Matthews, Eds. (Univ. of Arizona Press, Tucson, AZ, 1988), pp. 118–164.
6. S. C. Solomon *et al.*, *Science* **321**, 59 (2008).
7. S. L. Murchie *et al.*, *Science* **321**, 73 (2008).
8. T. R. Watters *et al.*, *Earth Planet. Sci. Lett.*; 10.1016/j.epsl.2009.01.025 (2009).
9. J. W. Head *et al.*, *Science* **321**, 69 (2008).
10. M. S. Robinson *et al.*, *Science* **321**, 66 (2008).
11. C. I. Fassett *et al.*, *Lunar Planet. Sci.* **40**, abstr. 1899 (2009)
12. R. G. Strom, C. R. Chapman, W. J. Merline, S. C. Solomon, J. W. Head, *Science* **321**, 79 (2008).
13. M. Cintala, R. A. F. Grieve, *Meteorit. Planet. Sci.* **33**, 889 (1998).
14. J. W. Head *et al.*, *J. Geophys. Res.* **98**, 17149 (1993).
15. B. W. Denevi *et al.*, *Science* **324**, 613 (2009).
16. S. C. Solomon, J. W. Head, *Rev. Geophys. Space Phys.* **18**, 107 (1980).
17. T. R. Watters, *J. Geophys. Res.* **93**, 10236 (1988).
18. M. P. Golombek, J. B. Plescia, B. J. Franklin, *Proc. Lunar Planet. Sci. Conf.* **21**, 679 (1991).
19. R. A. Schultz, *J. Geophys. Res.* **105**, 12035 (2000).
20. T. R. Watters, F. Nimmo, M. S. Robinson, *Geology* **33**, 669 (2005).
21. A. M. Freed, H. J. Melosh, S. C. Solomon, *J. Geophys. Res.* **106**, 20603 (2001).
22. H. J. Melosh, W. B. McKinnon, in *Mercury*, F. Vilas, C. R. Chapman, M. S. Matthews, Eds. (Univ. of Arizona Press, Tucson, AZ, 1988), pp. 374–400.
23. P. J. Kennedy, A. M. Freed, S. C. Solomon, *J. Geophys. Res.* **113**, E08004 (2008); 10.1029/2007JE002992.
24. A Mercury Dual Imaging System (MDIS) narrow-angle camera (NAC) mosaic at ~420 to 500 m per pixel and an 11-color WAC frame at ~5 km per pixel, obtained during the second MESSENGER flyby, revealed ~80% of the Rembrandt basin. The easternmost portion of the basin was imaged by MESSENGER during the first flyby at a comparable resolution.

25. We are grateful to the MESSENGER engineers and technical support personnel. The MESSENGER project is supported by the NASA Discovery Program under contracts NASW-00002 to the Carnegie Institution of Washington and NAS5-97271 to Johns Hopkins University Applied Physics Laboratory. This work is also supported by NASA grant NNX07AR60G.

Supporting Online Material

www.sciencemag.org/cgi/content/full/324/5927/618/DC1
SOM Text
Figs. S1 to S3
References

10 February 2009; accepted 9 April 2009
10.1126/science.1172109